Applied Acoustics 210 (2023) 109439

Contents lists available at ScienceDirect

Applied Acoustics

journal homepage: www.elsevier.com/locate/apacoust

A multibody dynamics approach on a tree-shaped acoustic black hole vibration absorber

Kaixing Huang [a], Yanni Zhang [a,*], Xiaoting Rui [a,*], Li Cheng [b,*], Qinbo Zhou [a]

[a] Institute of Launch Dynamics, Nanjing University of Science and Technology, Nanjing, Jiangsu, China
[b] Department of Mechanical Engineering, The Hong Kong Polytechnic University, Hung Hom, Kowloon, Hong Kong, China

ARTICLE INFO

Article history:
Received 17 December 2022
Received in revised form 1 May 2023
Accepted 12 May 2023

Keywords:
Acoustic black hole
Tree-shaped
Dynamic vibration absorber
Multibody system transfer matrix method
Robust low-frequency and broadband vibration reduction

ABSTRACT

Acoustic black hole (ABH) has shown great potential and aroused tremendous interest for vibration and sound control in the past two decades. However, efficient computational methods are still lacking for the design of ABH structures with practically required properties. Herein, a multibody system transfer matrix method is proposed to deal with a system comprising a host structure with an attached ABH cluster, exemplified by a novel tree-shaped ABH dynamic vibration absorber (ABH-DVA). Capitalizing on the flexibility offered by the method, the eigen-solutions and the steady-state vibration response of the combined system are derived and validated by finite element results. Observed vibration reduction and the underlying mechanisms are elucidated in terms of the vibrational energy ratio and vibration spatial distribution in the system. Owing to its rich modal dynamics and energy trapping capability, the proposed absorber demonstrates extraordinary and robust low-frequency and broadband vibration reduction performance from 25 Hz to 2500 Hz for different host structures. This can be ensured by designing its threshold frequency as the lower limit of the targeted frequency range. The proposed method and the vibration-reduction-effect are experimentally validated. This study offers a novel yet general approach for addressing complex ABH structures with various structural components and topologies.

1. Introduction

The use of dynamic vibration absorbers (DVAs) as add-on devices to a host structure is a common approach to suppress structural vibration. Ormondroyd and Den Hartog [1] showed the working principle of DVA by using a single degree of freedom (DOF) system. DVA can be broadly classified into discrete and continuous parameter types based on their structural configuration. The former is typically composed of mass-spring-damping elements with a single or a finite number of DOFs [2]. For broadband vibration control, multiple single DOF-DVA or a DVA with multiple DOFs are usually required and complex optimization are usually involved for determining their parameters [3–5]. In the latter category, plate- and shell-type absorbers are proposed to control the multi- modal vibrations of the host plate and shells [6,7]. Wang et al. reported a beam-type absorber with variable cross-section to absorb the vibration of a host plate [8]. Compared with the discrete parameter type DVA, the continuous parameter type DVA generally offers multi- and broadband modal control capabilities due to their rich dynamic properties.

In the 1980s, Ungar and Kurzweil first proposed viscoelastic waveguide absorbers [9] (WGA) for structural wave attenuation. Since then, various kinds of WGA have been proposed, such as viscoelastic beam type and plate type [10–12]. WGAs draw the vibration energy away from a structure through a proper design of waveguides with the aid of strong dissipative elements such as viscoelastic materials.

Despite their widespread use, both DVA and WGA suffer from some limitations in terms of effectiveness as well as design and implementation. The former, though simple in its structural form, often works at specific frequencies and requires tedious and complex parameter tuning. The latter usually has relatively weak dynamic coupling with the host structure and thus too often can hardly provide the required energy dissipation unless multiple absorbers with properly designed attachment locations are utilized. In addition, any changes in the host structure or environmental/operational conditions may jeopardize the effectiveness of both DVA and WGA.

During the last two decades, the phenomenon of the Acoustic Black Hole (ABH) has aroused great research interest in the field of vibration and noise control [13–20], due to its compactness,

* Corresponding authors.
E-mail addresses: yanni.zhang@njust.edu.cn (Y. Zhang), ruixt@163.net (X. Rui), li.cheng@polyu.edu.hk (L. Cheng).

https://doi.org/10.1016/j.apacoust.2023.109439
0003-682X/

lightweight and high energy-concentration properties. ABH allows for the manipulation of flexural wave propagation in a thin-wall structure by tailoring its thickness profile according to power law function, namely $h(x) = \varepsilon x^2 + h_0$, where ε is a constant and h_0 is the truncated thickness. When bending waves propagate into the ABH part, their phase velocity gradually decreases, and the wavelength is gradually compressed so that the wave amplitude increases accordingly alongside the gradual decrease of the structure thickness. As a result, energy is concentrated near the tip of the structure [21], which can then be effectively attenuated by a small amount of damping materials.

To cope with the robustness issue in conventional DVA design, ABH-featured absorbers embracing the combined DVA and WGA principles were first proposed by Zhou and Cheng in the form of a unilateral ABH-DVA [14]. The idea was further extended by Ji et al. to two-dimensional (2D) cases [22]. The proposed absorbers show broadband vibration suppression with relatively simple and easily achievable configuration. However, both studies were based on finite element (FE) analyses. In fact, this remains generally true for the large majority of works reported in the open literature, in which numerical tools like FE became the predominant means for ABH research. Although other methods like geometric acoustic methods, impedance analysis methods, and semi analytical methods [23–27] were also attempted, they typically apply to ABH structures with relatively simple geometries. For more complex ABH structures, numerical methods such as the finite element method or experimental methods are required [28,29]. More specific to the present topic, analytical/theoretical model of the host structure with ABH-DVAs has not been developed. In addition, as a distributed DVA, an in-depth investigation into different vibration reduction mechanisms in terms of the spatial distribution of vibration energy is essential to understand the energy transfer and distribution among different parts of the structure. Finally, there is a lack of effort in developing design guideline assisted by efficient simulation tools for achieving low frequency and broadband vibration reduction.

Herein, we provide an alternative to existing analysis methods based on multibody system transfer matrix method (MSTMM) for complex ABH-DVA design and analyses. MSTMM is an efficient multibody system dynamics method that has been proposed and gradually improved in the last two decades. The MSTMM is characterized by replacing the global dynamic equations with low-order transfer equations. Therefore, the matrix order involved in solving the dynamics of a multibody system is independent of the number of degrees of freedom of the system so that the computational efficiency can be greatly improved [30–32]. Besides, MSTMM does not require spatial discretization of the continuous elements when dealing with rigid-flexible coupled linear systems including beams, rods and shafts, and thus can accurately solve the system vibration characteristics and steady-state response. While the linear finite element method (FEM) uses polynomial functions etc. to interpolate the displacement at any point in the cell, which requires spatial discretization of the continuous elements and introduces additional approximations.

In this paper, a theoretical model of a combined structure consisting of a host structure with a tree-shaped ABH-DVA is developed and solved using the MSTMM with results validated by COMSOL FEM and experiments. Results show that the MSTMM substantially improves the computational efficiency for getting eigen-properties of the combined structure. Using the established model, we further explore the vibration reduction mechanisms of the ABH-DVA in terms of the spatial energy distribution. Based on the understanding acquired, a design strategy for achieving low-frequency and broadband vibration reduction is then proposed. The proposed tree-shaped ABH-DVA is shown to entail a denser modal density, resulting in wider absorption band and enhanced low frequency vibration reduction compared with the previous unilateral ABH-DVA. Meanwhile, the design demonstrates its robustness to accommodate different host structures without tedious tuning of the DVA parameters.

2. Dynamical equations by multibody system transfer matrix method

The proposed modelling approach is exemplified by a combined system consisting of a host structure and a tree-shaped ABH-DVA add-on, as shown in Fig. 1. Here the host structure can take any form. The tree-shaped ABH-DVA add-on consists of a connector and several ABH units which can be of different scales. Each ABH unit contains a tapered part, a uniform part, and a thin damping layer.

The basic idea of the MSTMM in solving the dynamics of the combined system is as follows: first, the combined system can be regarded as a complex multibody system and dismantled into elements with simple dynamic properties, such as rigid body, beam, etc. whose dynamic properties can be expressed by transfer matrix. Then, the overall transfer matrix of the system can be obtained by assembling these transfer matrices according to the topology of the system and the overall transfer equation (TE) of the system could be obtained accordingly. Next, the boundary conditions are substituted into the overall TE of the system to obtain the characteristic equation of the system, and the eigenfrequencies of the system are then obtained by solving the characteristic equation. The steady-state response of the system can also be obtained by solving the overall TE of the system with the load function [30].

To illustrate the process, a uniform cantilever beam is taken as the host structure onto which a tree-shape ABH-DVA consisting of four ABHs units (Fig. 2(a)) is attached. It should be noted, however, the modeling and analysis methods to be demonstrated is general and not limited to the beam case. As shown in Fig. 2(a), for each ABH unit, the thickness of the tapered part follows $h(x) = \varepsilon x^2 + h_0$($\varepsilon$ is a constant and $h_0 = 0.1$ mm), and a viscoelastic damping layer of constant thickness h_d is coated on the surface of the entire tapered region. All elements have the same width b (20 mm). A transverse excitation $F = \sin(\omega t)$ is applied at the free end of the host beam.

This specific combined system can be regarded as a bifurcated multibody system with eleven elements shown in Fig. 2(b). Elements 2, 6, 10 are the connection among different transmission paths which can be modelled as a virtual unit without mass [33]. Since low frequency vibration is concerned, Euler-Bernoulli beam theory is utilized for the host beam, the ABH-DVA and the connector. The state vector of elements j in the coordinate system $x_r - y_r$ is defined as $\mathbf{z}_{j,p}^r = [x, y, \theta_z, m_z, q_x, q_y]_{j,p}^T$, where p denotes input I or output O and $j = 1, 2, 3, ..., 11$; x and y denote linear displacements in the x and y directions; θ_z denotes angular displacements; q_x,q_y and m_z denote the forces and moments, respectively. The state vector in the associated modal coordinate[28] system can be expressed by $\mathbf{Z}_{j,p}^r = [X, Y, \Theta_z, M_z, Q_x, Q_y]_{j,p}^T$, where $\mathbf{z}_{j,p}^r = \mathbf{Z}_{j,p}^r e^{i\omega t}$ with ω being the angular frequency.

2.1. Transfer equations of elements

2.1.1. Transfer equation of an ABH unit

For an ABH unit shown in Fig. 3(a), since the transfer matrix of the variable-section beam cannot be obtained directly, each ABH unit can be considered as a series of beam segments (composite beam segment) of equal length which are connected sequentially, as shown in Fig. 3(b). For each beam segment comprised of a Euler

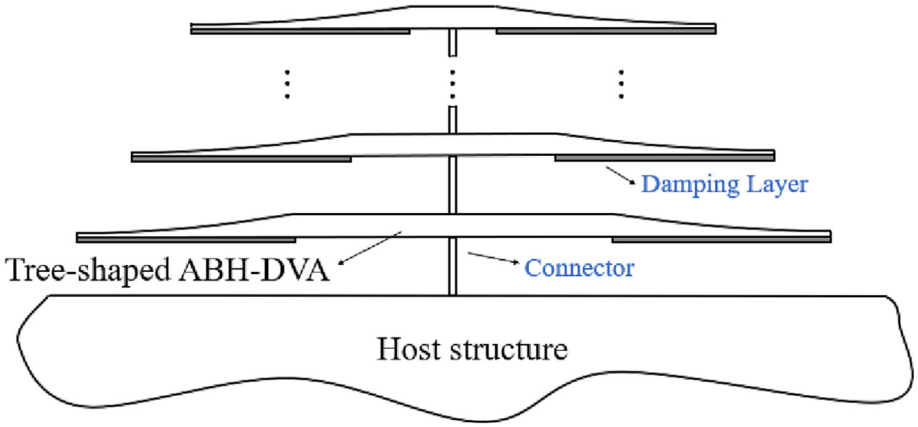

Fig. 1. A host structure with a tree-shaped ABH-DVA.

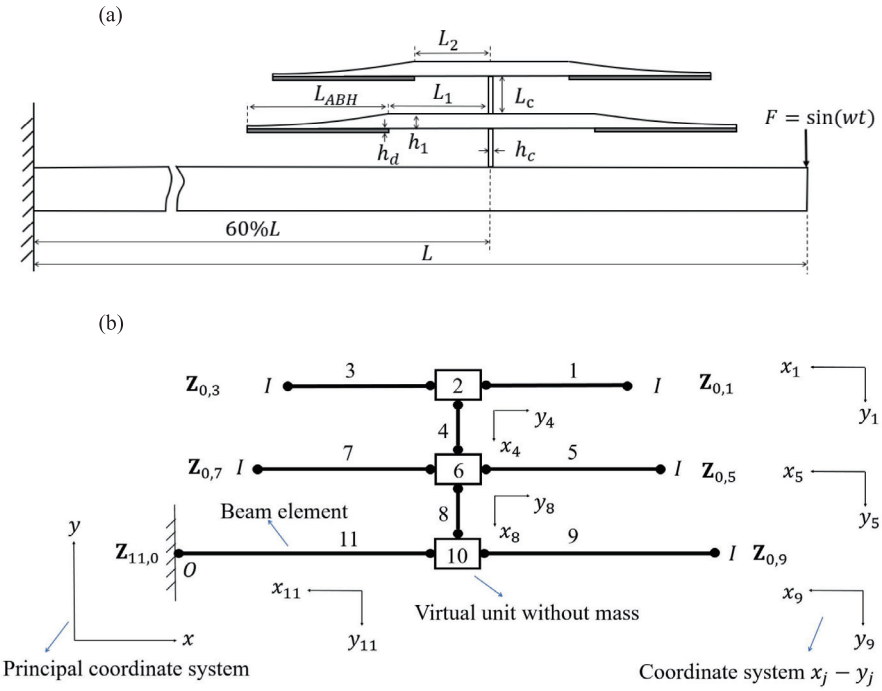

Fig. 2. (a) Schematic diagram of a host beam with a tree-shaped ABH-DVA, and 2(b) Planar bifurcation multibody system.

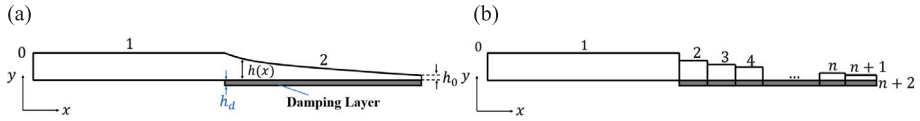

Fig. 3. Schematic cross section of ABH structure with damping layer. (a) Before simplification (b) After simplification.

Bernoulli beam and a damping layer, as shown in Fig. 4(a), Georgiev et al. expressed the flexural stiffness of the composite beam in plural form and took the additional mass of the damping layer into account when its thickness is comparable to or even larger than the thickness of the ABH [34].

The flexural stiffness and the linear density of beam segment writes:

$$EI(1+i\eta) = E_i I_i \left[(1+i\eta_i) + eH^3(1+i\eta_l) + \frac{3(1+H)^2 eH[1-\eta_i\eta_l + i(\eta_i+\eta_l)]}{1+eH(1+i\eta_l)} \right] \tag{2.1}$$

and

$$\bar{m} = \rho_i A_i + \rho_l A_l \tag{2.2}$$

where EI and $E_i I_i$ are the flexural stiffness of the composite beam and the beam itself, respectively;η is the material loss factor of the composite beam; η_i, E_i, h_i, ρ_i and A_i are the material loss factor, Young's modulus, thickness, density, and cross-sectional area of the beam itself; η_l, E_l, h_l, ρ_l and A_l are the material loss factor, Young's modulus, thickness, density, and cross-sectional area of the damping layer; $e = E_l/E_i$ is Young's modulus ratio, and $H = h_l/h_i$ is thickness ratio.

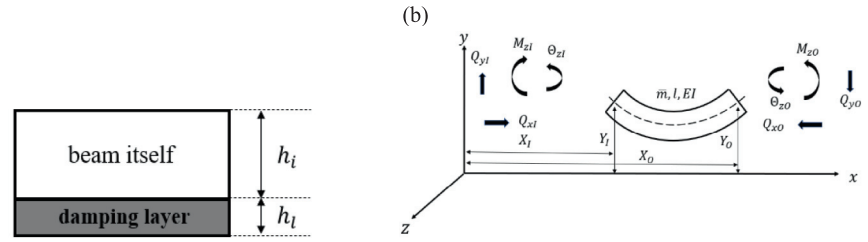

Fig. 4. (a) Schematic diagram of cross section of composite beam, and (b) Sign convention of the state vector of the beam element in MSTMM library [32].

$\mathbf{Z}_{0,1}, \mathbf{Z}_{1,2}, ..., \mathbf{Z}_{n+1,n+2}$ denote the state vectors of each connection point and $\mathbf{U}_i$ the transfer matrix of the ith segment of the beam. According to the positive sign convention shown in Fig. 4(b) and considering the beam transverse bending and longitudinal rigid body motion, the overall TE of the ABH unit can be obtained as:

$$\mathbf{Z}_{n+1,n+2} = \mathbf{U}_{n+1}\mathbf{U}_n \ \ldots \mathbf{U}_i \ \ldots \mathbf{U}_2\mathbf{U}_1\mathbf{Z}_{0,1} = \mathbf{U}\mathbf{Z}_{0,1} \tag{2.3}$$

where $\mathbf{U}_i (i = 1, 2, \ldots n+1)$ is the transfer matrix of the ith Euler-Bernoulli beam considering the transverse bending and longitudinal rigid body motion [30]:

$$\mathbf{U}_i = \begin{bmatrix} 1 & 0 & 0 & 0 & 0 & 0 \\ 0 & S(\lambda l) & \frac{T(\lambda l)}{\lambda} & \frac{U(\lambda l)}{EI\lambda^2} & 0 & \frac{V(\lambda l)}{EI\lambda^3} \\ 0 & \lambda V(\lambda l) & S(\lambda l) & \frac{T(\lambda l)}{EI\lambda} & 0 & \frac{U(\lambda l)}{EI\lambda^2} \\ 0 & EI\lambda^2 U(\lambda l) & EI\lambda V(\lambda l) & S(\lambda l) & 0 & \frac{T(\lambda l)}{\lambda} \\ \bar{m}\omega^2 l & 0 & 0 & 0 & 1 & 0 \\ 0 & EI\lambda^3 T(\lambda l) & EI\lambda^2 U(\lambda l) & \lambda V(\lambda l) & 0 & S(\lambda l) \end{bmatrix}_i \tag{2.4}$$

with

$$\lambda = \sqrt[4]{\bar{m}\omega^2/EI}, \begin{cases} S(x) = \frac{\cosh x + \cos x}{2}, T(x) = \frac{\sinh x + \sin x}{2} \\ U(x) = \frac{\cosh x - \cos x}{2}, V(x) = \frac{\sinh x - \sin x}{2} \end{cases} \tag{2.5}$$

Therefore, the transfer matrix of the ABH unit is obtained as $\mathbf{U} = \mathbf{U}_n \ldots \mathbf{U}_i \ldots \mathbf{U}_2\mathbf{U}_1$.

2.1.2. Transfer equations for other elements in the combined system

For element j ($j = 2, 6, 10$) or the massless virtual unit as a multiple input (N input) and single output elements, to obtain the corresponding TE in the principal coordinate system $x - y$, the kinematic and kinetic relationships need to be established. The motion continuity and force/moment balance of massless elements give:

$$X_{j,O} = X_{j,I_1}; Y_{j,O} = Y_{j,I_1}; \Theta_{j,zO} = \Theta_{j,zI_1}; M_{j,zO} = M_{j,I_1} + \ldots + M_{j,I_N};$$
$$Q_{j,xO} = Q_{j,xI_1} + \ldots + Q_{j,xI_N}, Q_{j,yO} = Q_{j,yI_1} + \ldots + Q_{j,yI_N}; (j = 2, 6, 10) \tag{2.6}$$

The above kinetic equations of elements can be synthesized as:

$$\mathbf{Z}_{j,0} = \mathbf{E}_6 \begin{bmatrix} X \\ Y \\ \Theta_z \\ M_z \\ Q_x \\ Q_y \end{bmatrix}_{j,I_1} + \begin{bmatrix} \mathbf{O}_3 & \mathbf{O}_3 \\ \mathbf{O}_3 & \mathbf{E}_3 \end{bmatrix} \begin{bmatrix} X \\ Y \\ \Theta_z \\ M_z \\ Q_x \\ Q_y \end{bmatrix}_{j,I_2} \ldots + \begin{bmatrix} \mathbf{O}_3 & \mathbf{O}_3 \\ \mathbf{O}_3 & \mathbf{E}_3 \end{bmatrix} \begin{bmatrix} X \\ Y \\ \Theta_z \\ M_z \\ Q_x \\ Q_y \end{bmatrix}_{j,I_N}$$
$$= \mathbf{U}_{j,I_1}\mathbf{Z}_{j,I_1} + \mathbf{U}_{j,I_2}\mathbf{Z}_{j,I_2} \ldots + \mathbf{U}_{j,I_L}\mathbf{Z}_{j,I_N} (j = 2, 6, 10) \tag{2.7}$$

The motion compatibility of different inputs yields the following geometric equations:

$$X_{j,I_1} = X_{j,I_2} = \ldots = X_{j,I_N}; Y_{j,I_1} = Y_{j,I_2} = \ldots = Y_{j,I_N}; \Theta_{j,zI_1} = \Theta_{j,zI_2}$$
$$= \ldots = \Theta_{j,zI_N} (j = 2, 6, 10) \tag{2.8}$$

which may be abbreviately written as geometric equations:

$$\mathbf{H}_{j,I_1}\mathbf{Z}_{j,I_1} = \mathbf{H}_{j,I_2}\mathbf{Z}_{j,I_2} = \ldots = \mathbf{H}_{j,I_N}\mathbf{Z}_{j,I_N} (j = 2, 6, 10) \tag{2.9}$$

where

$$\begin{bmatrix} 1 & 0 & 0 & 0 & 0 & 0 \\ 0 & 1 & 0 & 0 & 0 & 0 \\ 0 & 0 & 1 & 0 & 0 & 0 \end{bmatrix} = \mathbf{H}_{j,I_1} = \mathbf{H}_{j,I_2} = \ldots = \mathbf{H}_{j,I_N} (j = 2, 6, 10) \tag{2.10}$$

The TE of element j in the coordinate system $x_j - y_j$ is $\mathbf{Z}^j_{j,O} = \mathbf{U}^j_j\mathbf{Z}^j_{j,I} (j = 1, 3, 4, 5, 7, 8, 9, 11)$. The transfer matrix $\mathbf{U}^j_j (j = 1, 3, 5, 7)$ of the ABH unit in their respective coordinate systems can be obtained from Eqs. (2.1) to (2.5), and the transfer matrix $\mathbf{U}^j_j (j = 4, 8, 9, 11)$ of elements 4, 8, 9 and 11 in their respective coordinate systems can be obtained from Eqs. (2.4) and (2.5). The TE of the element j in the principal coordinate system are obtained from the following equations:

$$\mathbf{Z}_{j,O} = \mathbf{U}_j\mathbf{Z}_{j,I} (j = 1, 3, 4, 5, 7, 8, 9, 11) \tag{2.11}$$

where $\mathbf{U}_j = \left(\mathbf{A}^j\right)^{-1}\mathbf{U}^j_j\mathbf{A}^j$ is the transfer matrix of elements j in the principal coordinate system $x - y$, and $\mathbf{A}^j$ denotes the coordinate transformation matrix of the state vector from the coordinate system $x_j - y_j$ to the $x - y$. The TE of all elements in the principal coordinate system can then be obtained.

2.2. Overall transfer equations, steady state response and eigenvalues of the combined system

For a complex system containing multiple elements, the cumulative errors arising from the multiplication of a large number of transfer matrices may lead to computational stability problems, which can be solved by combining Riccati transformation with the MSTMM to form the reduced MSTMM [32,35,36] or RMSTMM [32,35].

The relationships among the state vectors of the multiple inputs (N input) and single output, and among the state vectors of multiple inputs (N input) of element j write, respectively [36]:

$$\mathbf{Z}_{j,O} = \sum_{k=1}^{N} (\mathbf{U}_{j,I_k}\mathbf{Z}_{j,I_k}) + \mathbf{f}_j \tag{2.12}$$

$$\mathbf{H}_{j,I_k}\mathbf{Z}_{j,I_k} = \mathbf{H}_{j,I_1}\mathbf{Z}_1 (k = 2, \ldots, N) \tag{2.13}$$

where $\mathbf{Z}_{m\times 1}$ is the state vector; $\mathbf{U}_{m\times m}$ is the transfer matrix; $\mathbf{H}_{m/2\times m}$ is the geometric equation coefficient matrix, and $\mathbf{f}_{m\times 1}$ is the load function array. In the present example, $L = 2$ for elements 2, 10 and $L = 3$ for element 6, $m = 6$. Riccati MSTMM chunks the state vector array of elements and Eqs. (2.12) and (2.13) can be rewritten as:

$$\begin{bmatrix} \mathbf{Z}_a \\ \mathbf{Z}_b \end{bmatrix}_{j,O} = \sum_{k=1}^{N} \left\{ \begin{bmatrix} \mathbf{T}_{aa} & \mathbf{T}_{ab} \\ \mathbf{T}_{ba} & \mathbf{T}_{bb} \end{bmatrix} \begin{bmatrix} \mathbf{Z}_a \\ \mathbf{Z}_b \end{bmatrix}_{j,I_k} \right\} + \begin{bmatrix} \mathbf{f}_a \\ \mathbf{f}_b \end{bmatrix}_j \tag{2.14}$$

$$[\mathbf{H}_a \quad \mathbf{H}_b]_{j,I_k}\begin{bmatrix}\mathbf{Z}_a\\ \mathbf{Z}_b\end{bmatrix}_{j,I_k} = [\mathbf{H}_a \quad \mathbf{H}_b]_{j,I_1}\begin{bmatrix}\mathbf{Z}_a\\ \mathbf{Z}_b\end{bmatrix}_{j,I_1} (k=2,\ldots,N) \tag{2.15}$$

At the boundaries of the system, the $\mathbf{Z}_a$ part contains $m/2$ zero elements, and the $\mathbf{Z}_b$ part contains the remaining $m/2$ unknown elements. Whether the state vector of intermediate connection points is divided into $\mathbf{Z}_a$ or $\mathbf{Z}_b$ is arbitrary. For N inputs, single output elements j, the Riccati transform of the state vector at the kth input is denoted as:

$$\mathbf{Z}_{a,j,I_k} = \mathbf{S}_{j,I_k}\mathbf{Z}_{b,j,I_k} + \mathbf{e}_{j,I_k} (k=1,2,\ldots,N) \tag{2.16}$$

Substituting Eq. (2.16) into Eqs. (2.14) and (2.15) yields the Riccati transformed form of the state vector at the output of a multiple inputs and single output element j as:

$$\mathbf{Z}_{a,j,O} = \mathbf{E}_a\mathbf{E}_b^{-1}(\mathbf{Z}_{b,j,O} - \mathbf{e}_b) + \mathbf{e}_a = \mathbf{S}_{j,O}\mathbf{Z}_{b,j,O} + \mathbf{e}_{j,O} \tag{2.17}$$

where

$$\begin{cases}\mathbf{S}_{j,O} = \mathbf{E}_a\mathbf{E}_b^{-1}\\ \mathbf{e}_{j,O} = \mathbf{e}_a - \mathbf{S}_{j,O}\mathbf{e}_b\end{cases} \tag{2.18}$$

$$\begin{cases}\mathbf{E}_a = \bar{\mathbf{U}}_{a,j,I_1} + \sum_{k=2}^{N}\bar{\mathbf{U}}_{a,j,I_k}\bar{\mathbf{H}}_{j,I_k}\\ \mathbf{e}_a = \bar{\mathbf{u}}_{a,j} + \sum_{k=2}^{N}\bar{\mathbf{U}}_{a,j,I_k}\bar{\mathbf{h}}_{j,I_k}\\ \mathbf{E}_b = \bar{\mathbf{U}}_{b,j,I_1} + \sum_{k=2}^{N}\bar{\mathbf{U}}_{b,j,I_k}\bar{\mathbf{H}}_{j,I_k}\\ \mathbf{e}_b = \bar{\mathbf{u}}_{b,j} + \sum_{k=2}^{N}\bar{\mathbf{U}}_{b,j,I_k}\bar{\mathbf{h}}_{j,I_k}\end{cases} \tag{2.19}$$

$$\begin{cases}\bar{\mathbf{U}}_{a,j,I_k} = \mathbf{T}_{aa,j,I_k}\mathbf{S}_{j,I_k} + \mathbf{T}_{ab,j,I_k}\\ \bar{\mathbf{U}}_{b,j,I_k} = \mathbf{T}_{ba,j,I_k}\mathbf{S}_{j,I_k} + \mathbf{T}_{bb,j,I_k}\\ \bar{\mathbf{u}}_{a,j} = \mathbf{f}_{a,j} + \sum_{k=1}^{N}\mathbf{T}_{ba,j,I_k}\mathbf{e}_{j,I_k}\\ \bar{\mathbf{u}}_{b,j} = \mathbf{f}_{b,j} + \sum_{k=1}^{N}\mathbf{T}_{ba,j,I_k}\mathbf{e}_{j,I_k}\end{cases} \tag{2.20}$$

$$\begin{cases}\bar{\mathbf{H}}_{j,I_k} = (\mathbf{H}_{a,j,I_k}\mathbf{S}_{j,I_k} + \mathbf{H}_{b,j,I_k})^{-1}(\mathbf{H}_{a,j,I_1}\mathbf{S}_{j,I_1} + \mathbf{H}_{b,j,I_1})\\ \bar{\mathbf{h}}_{j,I_k} = (\mathbf{H}_{a,j,I_k}\mathbf{S}_{j,I_k} + \mathbf{H}_{b,j,I_k})^{-1}(\mathbf{H}_{a,j,I_1}\mathbf{e}_{j,I_1} - \mathbf{H}_{a,j,I_k}\mathbf{e}_{j,I_k})\end{cases} \tag{2.21}$$

where $\mathbf{E}_a$, $\mathbf{E}_b$, $\mathbf{e}_a$, $\mathbf{e}_b$ satisfy:

$$\mathbf{Z}_{b,j,I_k} = \bar{\mathbf{H}}_{j,I_k}\mathbf{Z}_{b,j,I_1} + \bar{\mathbf{h}}_{j,I_k} (k=2,3,\ldots,L) \tag{2.22}$$

$$\mathbf{Z}_{a,j,O} = \mathbf{E}_a\mathbf{Z}_{b,j,I_1} + \mathbf{e}_a \tag{2.23}$$

$$\mathbf{Z}_{b,j,O} = \mathbf{E}_b\mathbf{Z}_{b,j,I_1} + \mathbf{e}_b \tag{2.24}$$

Eq. (2.18) is the recurrence equation for $\mathbf{S}$ and $\mathbf{e}$ of elements 2, 6, 10. The recursive equations of $\mathbf{S}$ and $\mathbf{e}$ for single input and single output elements 1, 3, 4, 5, 7, 8, 9 and 11 can be simplified by removing the redundant inputs and the terms of the geometric equations in Eqs. (2.12) to (2.21).

$$\begin{cases}\mathbf{S}_{j,O} = (\mathbf{T}_{aa,j}\mathbf{S}_{j,I} + \mathbf{T}_{ab,j})(\mathbf{T}_{ba,j}\mathbf{S}_{j,I} + \mathbf{T}_{bb,j})^{-1}\\ \mathbf{e}_{j,O} = (\mathbf{T}_{aa,j}\mathbf{e}_{j,I} + \mathbf{f}_{a,j}) - \mathbf{S}_{j,O}(\mathbf{T}_{ba,j}\mathbf{e}_{j,I} + \mathbf{f}_{b,j})\end{cases} \tag{2.25}$$

In the bifurcated multibody system shown in Fig. 2(b), each input of the system corresponds to $\mathbf{Z}_a = \mathbf{0}$ and $\mathbf{Z}_b \neq \mathbf{0}$, then at the input side $\mathbf{S} = \mathbf{0}$ and $\mathbf{e} = \mathbf{0}$. $\mathbf{S}$ and $\mathbf{e}$ at each intermediate connection point of the system and $\mathbf{S}_{11,O}$ and $\mathbf{e}_{11,O}$ at the output can be obtained recursively from Eqs. (2.18) and (2.25). Boundary condition $\mathbf{Z}_{a,11,O} = \mathbf{0}$ at the output of the system is then substituted into Eq. (2.17) to solve for the unknown variables in the state vector at the output of the system. After obtaining the state vector at the output of the system, the state vector of any connection point of the system can be obtained from Eqs. (2.16), (2.22) and (2.24), as shown in Fig. 5.

The above procedure gives the solution to the steady state response of the bifurcated multibody system shown in Fig. 2(b). As to the associate eigenvalue problem, by removing the external excitation in the above categories, the characteristic equation of the bifurcated multibody system is obtained as $\Delta(\omega) = \det \mathbf{S}_{11,O} = 0$, where det denotes the determinant of a matrix. However, the solution when the determinant of matrix $\mathbf{E}_b$ or $\mathbf{T}_{ba,j}\mathbf{S}_{j,I} + \mathbf{T}_{bb,j}$ equals zero is the pole of the characteristic equation $\Delta(\omega)$. If the root-seeking method based on symbol change such as dichotomy is directly adopted, these poles would be mistakenly taken as the roots of the equation [37]. To tackle this problem, the $\bar{\mathbf{U}}_{b,j,I_k}$ is written as Φ_{j,I_K} and $(\mathbf{H}_{a,j,I_k}\mathbf{S}_{j,I_k} + \mathbf{H}_{a,j,I_k})$ is written as Ψ_{j,I_k} to obtain the general form of the characteristic equation of the bifurcation system [37]

$$\det \mathbf{U}_{RTMM} = |\mathbf{S}_{n,0}|\prod_{j=1}^{n}|\Gamma_j| \tag{2.26}$$

where n is the element number at the system output, and the expression of $|\Gamma_j|$ is as follows:

$$\begin{cases}|\Phi_j| & (\text{single input})\\ \left|\Phi_{j,I_1} + \left(\sum_{k=2}^{N}\Phi_{j,I_1}\Psi_{j,I_k}^{-1}\right)\Psi_{j,I_1}\right|\prod_{k=2}^{N}|\Psi_{j,I_k}| & (\text{multiple input})\end{cases} \tag{2.27}$$

$|\mathbf{S}_{n,0}|\prod_{j=1}^{n}|\Gamma_j|$ avoids the influence of zero denominator in $|\mathbf{S}_{n,0}|$. As a result, the eigenfrequencies can be solved directly using the

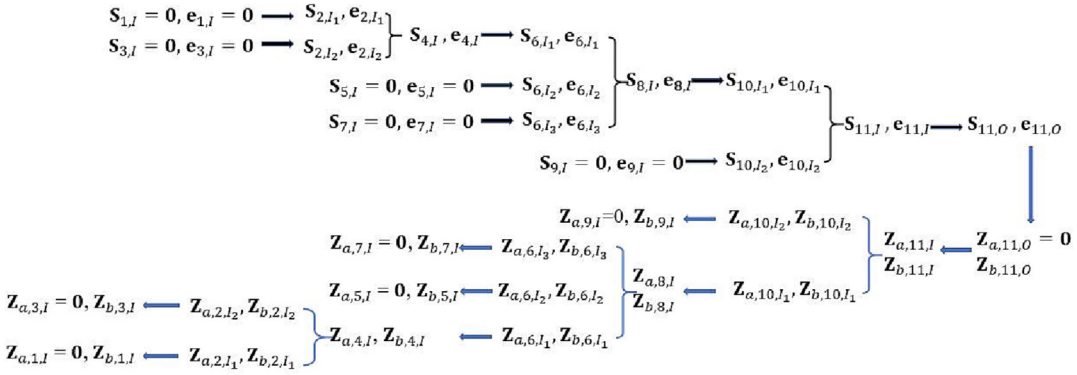

Fig. 5. Calculation process of steady state response of combined system based on Riccati MSTMM.

dichotomy method or recursive eigenvalue search algorithm [38]. The characteristic equation of the linear bifurcated multibody system shown in Fig. 2(b) can be expressed by:

$$\det \mathbf{U}_{RTMM} = |\mathbf{S}_{11,0}| \prod_{j=1}^{11} |\Gamma_j| \tag{2.28}$$

The eigenfrequencies of the bifurcated multibody system of Fig. 2(b) can be obtained by solving Eq. (2.28).

3. Vibration reduction and mechanisms analyses

3.1. Model validation

For model validation, the results calculated from the proposed MSTMM are compared with the COMSOL finite element simulation results calculated using the solid mechanics module. In order to simplify the model, set the four ABH units in Fig. 2 (a) as the same. A FE model of the combined system consisting of a host beam with tree-shaped ABH-DVA shown in Fig. 2(a) is established. The convergence is reached when the errors of the first fifteen eigenfrequencies of the system are all within 1% as the density of the grid gradually increases. The coating attached to the ABH is a viscoelastic material and the rest of the system is aluminum. The detailed material and geometric parameters of each part of the combined system are listed in Table 1.

Comparisons in terms of eigenfrequencies are shown in Table 2, where n is the number of segments of the ABH-DVA tapered part, t is the calculation time, and the relative error is calculated by $\sigma = (f_{\mathrm{MSTMM}} - f_{\mathrm{FEM}})/f_{\mathrm{FEM}}$.

Table 2 shows that the relative errors of the eigenfrequencies using the MSTMM and the FEM in COMSOL are generally small and are getting smaller as the number of segments increases. The relative error of the first fifteen eigenfrequencies when $n = 200$ is within 3.45%, which demonstrates the correctness of the proposed method. Although the computation time becomes longer for a larger number of segments, the computation time by MSTMM is still less than that by FEM, typically one tenth of that by FEM when the number of segments reach 200. That is, MSTMM significantly reduces the computation time.

Next, the steady state responses calculated by the two methods are compared. To ensure the convergence of the calculation results by both methods, the tapered part of ABH-DVA is divided into 200 segments, and the calculation frequency interval is taken as 0.1 Hz. The driving point mobility ($Mobility = 20\log j\omega Y/F$) of the system at the excitation point is calculated using the two methods and compared in Fig. 6, showing good agreement except at higher frequencies where the response curves are similar in trend but slightly shifted in frequency position. This is expected since in the MSTMM, Euler Bernoulli beam theory is used which neglects the rotational inertia and shear deformation, which results in a slight overestimation of the eigenfrequencies at higher frequencies; while FEM solid mechanics module result is based on the linear elasticity. To reduce the difference in accuracy at high frequencies between the two methods, the Timoshenko beam theory could be used in the MSTMM by replacing the transfer matrix of the Euler-Bernoulli beam with that of the Timoshenko beam, which can be referred to Ref. 30. Nevertheless, the amplitudes of the resonance peaks corresponding to the same eigenfrequency are basically the same, which demonstrate the correctness of the proposed method.

3.2. Vibration reduction and associated mechanisms

To evaluate the vibration reduction performance of the tree-shaped ABH-DVA, the driving point mobility of the combined system is shown in Fig. 7 using MSTMM, with the counterpart response without absorber being used as a reference. The loss fac-

Table 1
Material and geometric parameters of the combined system.

Material parameters			Geometric parameters			
aluminum	E_a	70 GPa	L	600 mm	h_c	3 mm
	ρ_a	2700 kg/m^3	L_1	50 mm	h_d	1 mm
	η_1	0.001	L_2	50 mm	h	16 mm
Damping layer	E	30 MPa	L_{ABH}	50 mm	h_1	3 mm
	ρ	980 kg/m^3	L_c	16 mm		
	η_2	0.3				

Table 2
Comparison of eigenfrequencies calculated by MSTMM and FEM in COMSOL.

Mode number	MSTMM						FEM in COMSOL
	n = 10		n = 50		n = 200		
	f/(Hz)	σ/%	f/(Hz)	σ/%	f/(Hz)	σ/%	f/(Hz)
1	34.82	−0.37	34.96	0.03	34.97	0.06	34.95
2	159.77	0.59	159.48	0.41	159.21	0.24	158.83
3	213.42	−0.18	214.05	0.12	214.15	0.16	213.80
4	295.36	−0.81	300.23	0.83	300.49	0.91	297.77
5	366.99	0.13	366.31	−0.06	364.46	−0.56	366.52
6	384.69	1.21	381.36	0.34	378.81	−0.33	380.08
7	625.56	18.49	566.14	7.24	546.16	3.45	527.93
8	662.94	14.46	609.71	5.27	590.73	1.99	579.19
9	719.75	19.91	615.02	2.46	608.89	1.44	600.23
10	757.08	20.33	653.77	3.91	634.69	0.88	629.15
11	772.40	15.29	685.90	2.38	678.85	1.33	669.96
12	982.57	12.81	908.51	4.31	896.34	2.91	870.97
13	1251.75	1.11	1250.24	0.99	1249.80	0.95	1238.00
14	1672.63	14.56	1525.66	4.50	1493.61	2.30	1460.00
15	1805.23	15.52	1634.44	4.59	1594.88	2.06	1562.70
t/s	0.18		0.26		0.41		5

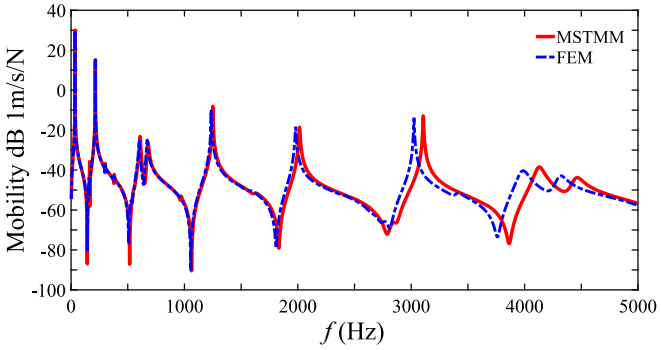

Fig. 6. Comparison of the driving point mobility calculated by MSTMM and FEM.

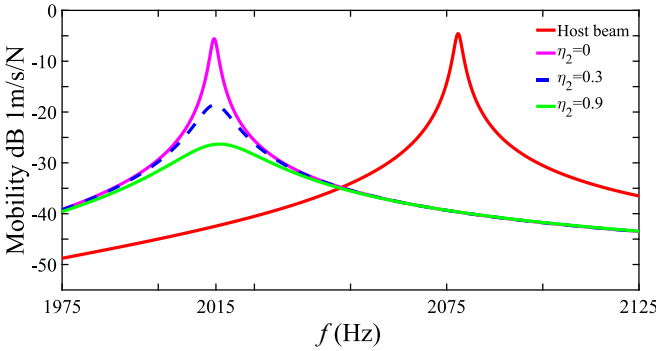

Fig. 8. Driving point mobility of the combined system with different damping layer loss factors: near the 5th resonance peak; driving point mobility of the host beam without ABH-DVA acts as a reference.

tor of the damping layer is set as $\eta_2 = 0.3$ as indicated in Table 1 alongside other system parameters.

Fig. 7 shows that, with the introduction of the tree-shaped ABH-DVA, most of the resonance peaks are suppressed except for the first two ones, indicating that the ABH add-on can effectively suppress the vibration of the host beam. Based on the peak vibration suppression, the resonance peaks can be divided into four categories: resonance peak reduction without splitting (e.g., 4th and 5th ones), resonance peak reduction with splitting (e.g., 3rd and 7th ones), low frequency resonance peaks with almost no changes (e.g., 1st and 2nd ones), and resonance peaks without obvious vibration reduction (e.g., 6th one). To investigate the underlying physical mechanisms, some typical peaks are selected and scrutinized.

For the first category, the mobility variation of the 5th resonance peak with different loss factors is shown in Fig. 8. It can be seen that, without damping, the frequency position and mobility amplitude at the peak hardly change. A damping increase leads to a reduction of the mobility amplitude with gradually broadened bandwidth. Therefore, this peak reduction can be attributed to the increased modal damping with the introduction of the ABH-DVA attached with a damping layer, which can be classified as "damping dominated"[14].

Examining the variation of the 3rd resonance peak as an example of the second category, the original resonance peak is obviously split into two peaks, similar to a conventional single DOF-DVA. This is due to the strong coupling/interaction between the ABH-DVA and the host beam at this frequency where their eigenfrequencies match. Gradually increasing the loss factor of the damping layer, the amplitudes of the resonance peaks decrease rapidly before reaching a smooth and flattened region (Fig. 9), while the response curves at different loss factors intersect at two fixed points P and Q, satisfying the well-known fixed-point theory [39] of conventional DVAs. The modal loss factor at this frequency is significantly enhanced from about 0.001 to 0.04, as to be further demonstrated later in Fig. 15. The peak reduction at this point is thus the result of the combined effect of strong interaction and enhanced damping [14].

However, for the same damping case ($\eta_2 = 0.3$), the decrease in amplitude of the 5th resonance peak (14 dB, Fig. 8) is much smaller than that of the 3rd resonance peak (28 dB, Fig. 9). This means the vibration reduction under the frequency matching condition is substantially increased. To further investigate the physical mechanisms behind the difference in vibration reduction, the vibration energy at different parts of the combined system is investigated. To clarify the effect of structural interaction alone, the damping layer loss factor η_2 is set to zero to avoid the effect of energy loss. The kinetic energy of the host beam E_{Host} and that of the ABH-DVA $E_{ABH-DVA}$ (ignoring the vibration energy of the connector due to its much smaller vibration energy relative to that of the ABH unit and the host beam) at these two resonant frequencies are calculated. The associated kinetic energy ratio $\Gamma = 10\log(E_{ABH-DVA}/E_{Host})$ is thus obtained, are shown in Fig. 10. The spatial distributions of the associated root mean square (RMS) velocity at these two frequencies are shown in Fig. 11.

Fig. 10 shows that Γ_{3rd} (0.73 dB) is about 9 dB higher than Γ_{5th} (-8.25 dB). Therefore, a greater amount of vibration energy is transferred from the host beam to the ABH-DVA due to the strong interaction between them when their eigenfrequencies are matched. Meanwhile, Fig. 11 shows that, for both frequencies, the velocity amplitude at the ABH tapered section is much higher

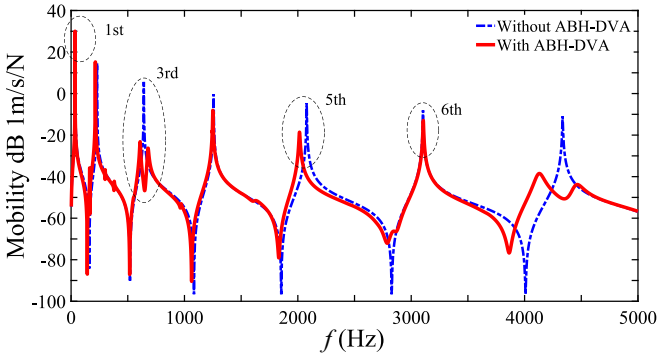

Fig. 7. Driving point mobility of the host beam with and without tree-shaped ABH-DVA.

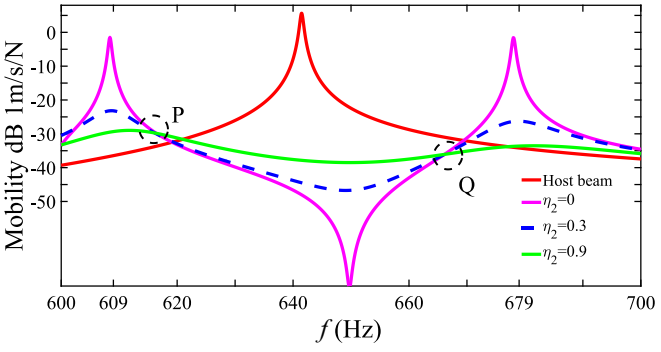

Fig. 9. Driving point mobility of the combined system with different damping layer loss factors: near the 3rd resonance peak; driving point mobility of the host beam without ABH-DVA acts as a reference.

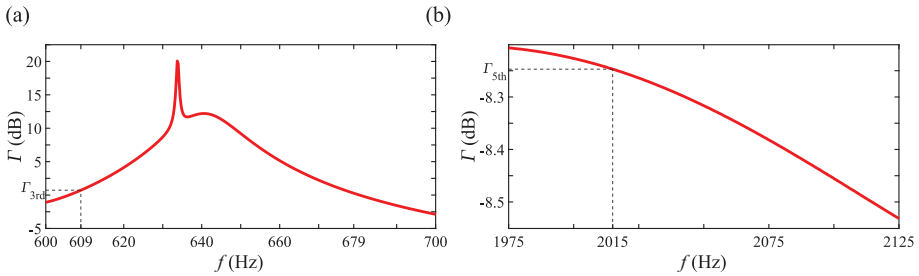

Fig. 10. Kinetic energy ratio of ABH-DVA to that of the host beam near the (a) 3rd and (b) 5th resonance frequencies.

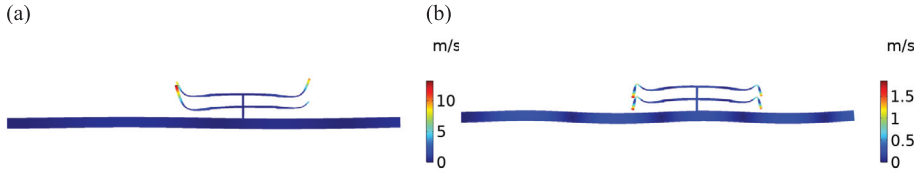

Fig. 11. Spatial distribution of the root mean square (RMS) velocity at the (a) 3rd and (b) 5th resonance frequencies.

than that of the rest of the structure, indicating an ABH-specific energy concentration in both cases, thus leading to a significant enhancement of the system damping at both frequencies. However, the velocity amplitude of the ABH tapered section at the 3rd resonance frequency (Fig. 11(a)) is much larger compared with that of the 5th resonance frequency (Fig. 11(b)) due to the strong interaction effect at the frequency matching conditions. As a result, the energy concentrated in the ABH tapered part at the 3rd resonance frequency is much higher, resulting to a more significant damping increase and vibration reduction.

For the third category, exemplified by the 1st resonance peak, the original resonance peak does not drop when the ABH-DVA is added, even with a very large damping loss factor of the layer (Fig. 12(a)). To understand the reason for the absence of energy loss increase in the system, the spatial distribution of the RMS velocity of the combined system at this frequency ($f = 35$ Hz) with $\eta_2 = 0.9$ is shown in Fig. 12(b). One can see that no local modal response is excited in the tapered part of the ABH unit and the whole ABH unit acts as a rigid body moving with the host beam. This is because this frequency is well below the threshold frequency (f_{et}) at which the ABH effect starts to take systematic effects [40], featuring a sudden increase of the modal loss factor of the ABH structure. This typically happens when the length of the tapered profile L_{ABH} gets close to the quarter wavelength of

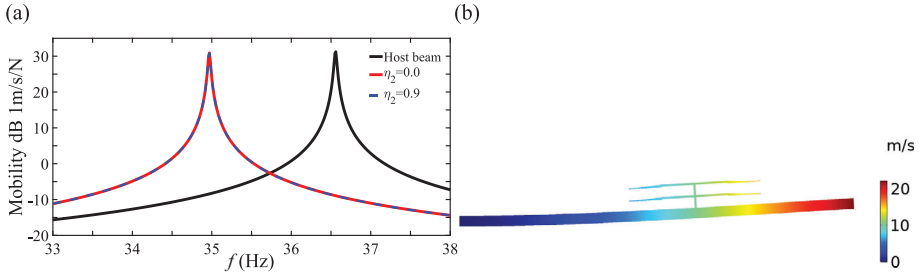

Fig. 12. (a) Driving point mobility of the combined system with different damping layer loss factors: near the 1st resonance peak; driving point mobility of the host beam without ABH-DVA acts as a reference. (b) Spatial distribution of root means square (RMS) velocity at the 1st resonance frequencies ($f = 35$ Hz) with $\eta_2 = 0.9$.

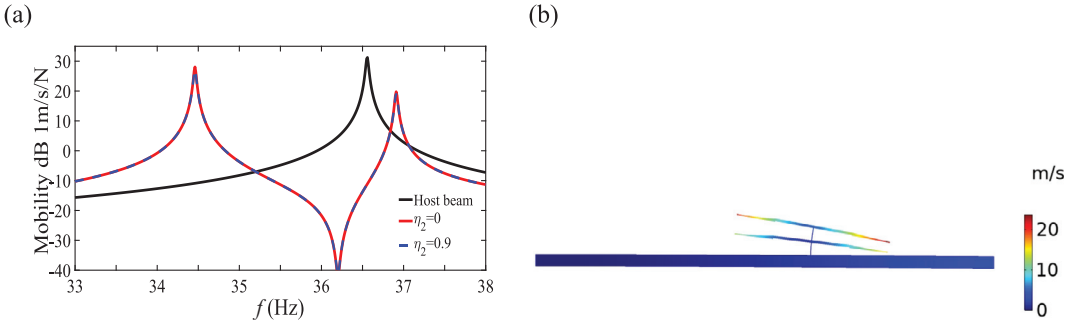

Fig. 13. (a) Driving point mobility of the combined system with different damping layer loss factors at the 1st resonance peak frequency matching; driving point mobility of the host beam without ABH-DVA acts as a reference. (b) Root means square spatial distribution of velocity at the 1st resonance frequencies ($f = 34.5$ Hz) with $\eta_2 = 0.9$.

the incoming waves estimated over the homogeneous region of the beam at f_{et}, i.e., $L_{ABH} = 0.25 \times 2\pi\sqrt[4]{Eh^2/12\rho(2\pi f_{et})^2}$. Here $f_{et} = 692$ Hz. Hence at this frequency, the modal loss factor of the system hardly increases as to be further quantified in Fig. 15. Actually, the ABH acts as a rigid mass added to the host beam so that the resonance frequency of the system shifts to a lower frequency, with the amplitude of the resonance peak nearly unchanged.

To further demonstrate whether low frequency resonance peaks below f_{et} can be reduced when strong structural interaction is present, a frequency matching condition is created by adjusting the eigenfrequency of ABH-DVA via increasing the size of the connector h_c while keeping the ABH unit unchanged. When $h_c = 1$ mm, frequency matching occurs at the first resonance peak, as shown in Fig. 13(a). The corresponding structural deformation is plotted in Fig. 13(b).

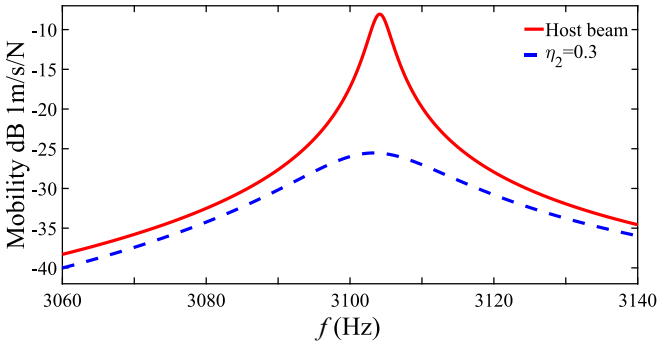

Fig. 14. The driving point mobility near the 6th resonance peak after changing the installation position; driving point mobility of the host beam without ABH-DVA acts as a reference.

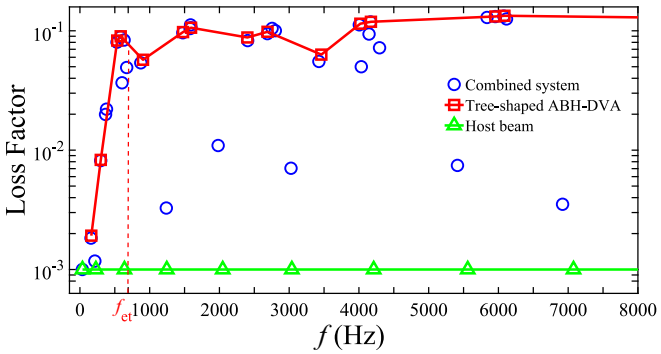

Fig. 15. Loss factors of different systems: the host beam alone, tree-shaped ABH-DVA, combined system (all fixed-free,$\eta_2 = 0.9$), and the configurations of different system elements are the same as those in Fig. 7.

Fig. 13(a) shows that when the eigenfrequency of the host beam matches that of the ABH-DVA, the first resonance peak splits into two with their amplitudes reduced by approximately 5 dB and 12 dB respectively. It is noted that this vibration reduction varies little with the increase of damping loss factor. Fig. 13(b) shows that the ABH unit is moving as a whole like a single degree of freedom dynamic vibration absorbers (SDOF-DVA), with most of the vibration energy transferred from the host beam to the upper branches of the ABH-DVA. So, the driving point mobility amplitude decreases. The associated mechanism can thus be attributed to a pure "interaction-dominated" phenomenon and the loss effect of the damping layer could hardly work due to the little deformation of the ABH at such a low frequency below f_{et}.

For the fourth category exemplified by the 6th resonance peak, no vibration reduction can be achieved. This is because the installation position of ABH-DVA (0.6L) is near a nodal position of the 6th-order transverse vibration mode of the host beam, making it difficult to generate energy transfer from the host beam to ABH-DVA [5,14]. The vibration reduction effect can be achieved by changing the installation position, as shown in Fig. 14, where the ABH-DVA installation position is moved to 0.55L to successfully entail a vibration reduction of the resonance peak.

The above analyses on the amplitude drop of different types of formants indicate that the observed phenomena are largely related to ABH characteristics. To better illustrate this point, the modal distribution, and the corresponding loss factors of the host beam alone as a uniform beam, the ABH-DVA and the combined system are shown in Fig. 15. It can be seen that the modal loss factor of the tree-shaped ABH-DVA is small at low frequencies. From about 600 Hz onwards, the loss factor increases abruptly to a higher level. This frequency starting from which the loss factor increases abruptly is basically consistent with the f_{et} proposed by Denis et al. [40]. That is, with the addition of the ABH add-on, the loss factor of the combined system increases substantially near and above f_{et}, where a significant vibration reduction effect can be achieved with less damping material. Especially, when the eigenfrequencies of the host beam match those of the ABH-DVA, the loss factor of the combined system is also significantly enhanced. Note that in this section, the kinetic energy ratio, the velocity spatial distribution and loss factor figures, Figs. 10, 11, 12(b), 13(b) and 14 are from

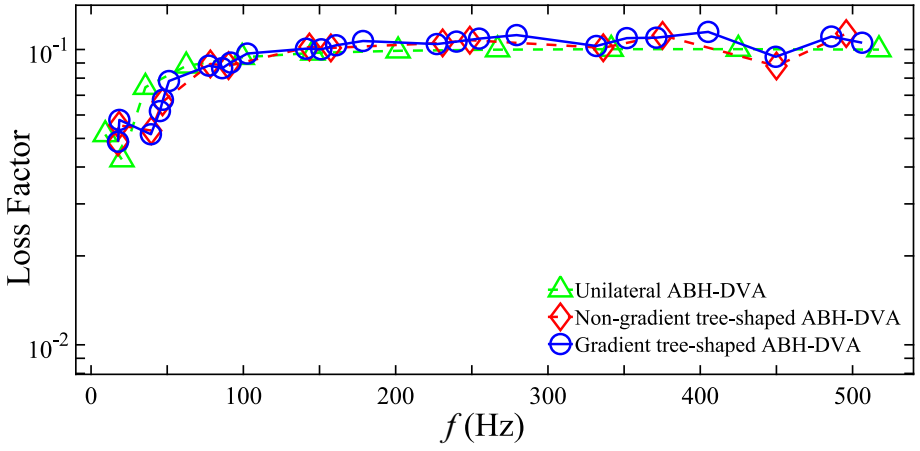

Fig. 16. Comparison of modal loss factors between non-gradient tree-shaped ABH-DVA, gradient tree-shaped ABH-DVA and unilateral ABH-DVA with the same mass and damping material.

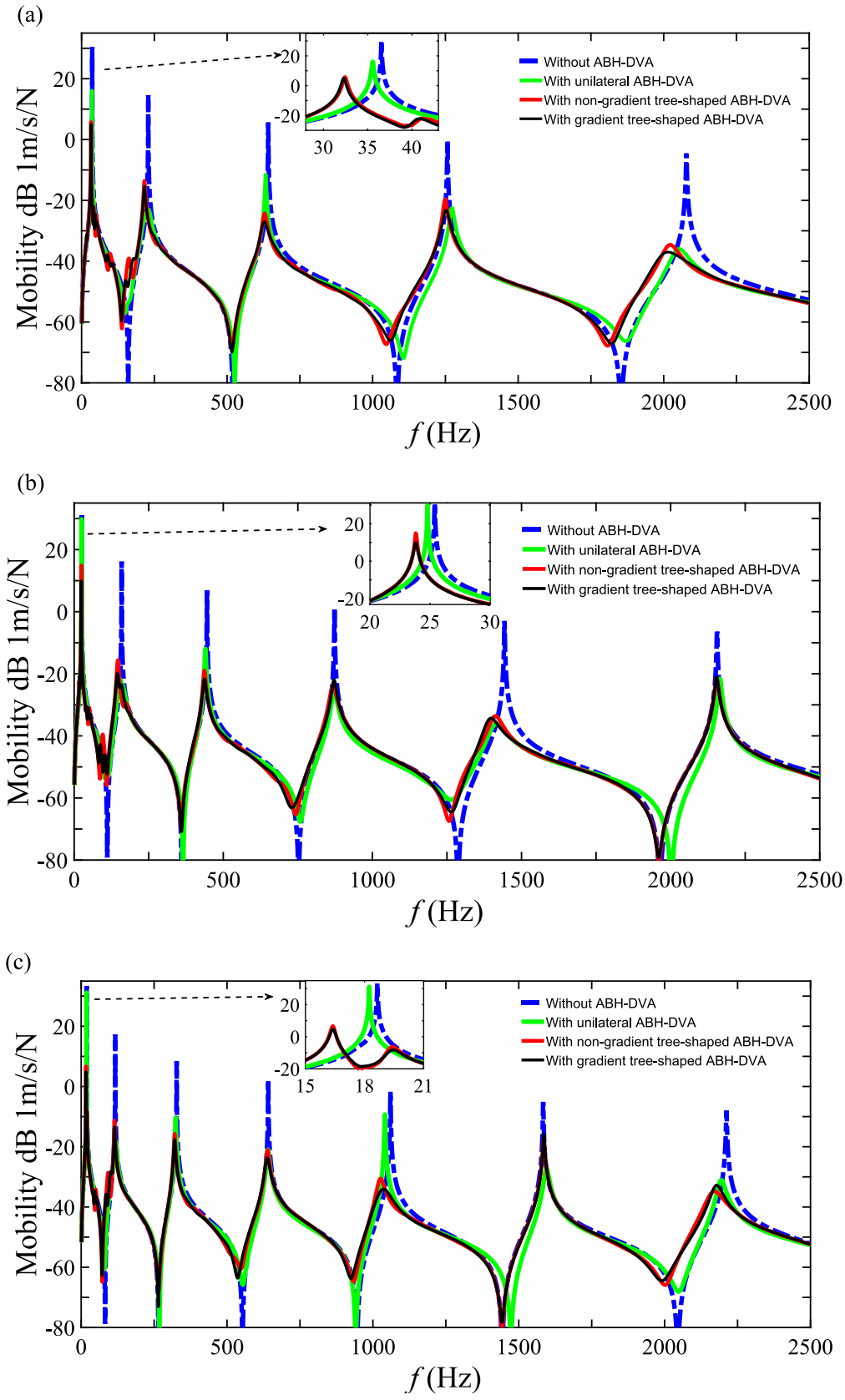

Fig. 17. Driving point mobility of the host beam with non-gradient tree-shaped, gradient tree-shaped and unilateral ABH-DVAs for different dimension of the host beams, with that of same host beam without ABH-DVA as a reference: (a)$L = 0.6$ m (b)$L = 0.72$ m and (c)$L = 0.84$ m, and the configurations of different DVA are the same as those used in Fig. 16.

COSMOL FEM to offer a better visualization. All the other figures are based on the MSTMM.

4. Robust low-frequency and broadband vibration reduction

4.1. ABH-DVA for low-frequency and broadband vibration mitigation

Previous analyses demonstrate that the ABH-DVA can entail systematic vibration reduction above its threshold frequency, while the effect is less obvious when frequency matching conditions are not satisfied due to the limited amount of concentrated vibration energy. Besides, at low frequencies below or near threshold frequency, where the ABH effect is poor, it is difficult to achieve effective vibration reduction by relying solely on the ABH or DVA effect. However, through a combined control of ABH effect and strong interaction of DVA, vibration reduction effect can be greatly enhanced.

This understanding alludes to the possibility of increasing the modal density of the DVA so that more ABH-DVA's eigenfrequencies can match with those of the host beam to generate better vibration reduction effects. To demonstrate this, low-frequency broadband vibration reduction in the range of 25 Hz-2500 Hz is targeted with the help of a tree-shaped ABH-DVA containing four branches of ABH unit. First of all, the threshold frequency f_{et} of the ABH-DVA is set to be equal to the lower bound of the concerned frequency range, i.e. 25 Hz. A simple way is to adjust the length of the tapered part L_{ABH} of each ABH branch by the rule of thumb provided by Denis et al. [40]:

$$L_{ABH} = 0.25 \times 2\pi \sqrt[4]{Eh_1^2/12\rho(2\pi f_{et})^2} \tag{4.1}$$

This yields $L_{ABH} = 260$ mm when $f_{et} = 25$ Hz.

As a result, the longer tapered section of ABH lowers the threshold frequency and increases the number of local modes at low frequencies, especially in the present tree-shaped configuration. This would favor the eigenfrequency matching between the DVA and the main structure. This is demonstrated by Fig. 16, which compares the loss factors of the proposed tree-shaped ABH-DVA of two types with those of the unilateral counterpart. The first type is a non-gradient tree-shaped ABH-DVA with four identical ABH units ($L_1 = L_2 = 50$ mm), and the second type is a gradient tree-shaped ABH-DVA with gradiently and linearly varied branch length ($L_1 = 75$ mm, $L_2 = 25$ mm), with the taper length L_{ABH} of both types 260 mm as calculated by Eq. (4.1). The unilateral ABH-DVA has only one ABH branch whose relevant sizes L_1, h_1 and L_{ABH} are twice as large as those of the non-gradient tree-shaped ABH-DVA, with other parameters being kept the same as those in Table 1. The mass and damping materials of the above three ABH-DVAs are kept the same, with $\eta_2 = 0.6$.

Fig. 16 shows that the loss factors of proposed non-gradient tree-shaped, gradient tree-shaped and unilateral ABH-DVAs are all high in the frequency range from 0 Hz to 500 Hz. For the same additional weight and damping material of the ABH-add on, the two types of tree-shaped ABH-DVAs exhibit much higher modal density than the unilateral one, especially the gradient tree-shaped ABH-DVA, which increases the chance of frequency matching. Thus, the tree-shaped ABH-DVA, especially the gradient one, is expected to have better vibration reduction performance, which will be demonstrated in the following section.

4.2. Robust vibration reduction for different host structures

To verify the vibration reduction effect of the gradient tree-shaped ABH-DVA and its robustness in coping with structural changes in the host structure, the two types of tree-shaped ABH-DVAs are installed on three different host beams. At the same time, the unilateral ABH-DVA combined system with the same mass and damping material is taken as a reference for comparison in Fig. 17.

Fig. 17 shows that for the three different host beams, these two tree-shaped ABH-DVAs provide good vibration reduction for almost all resonance peaks in the range of 25 Hz-2500 Hz (except for some resonance peaks due to the installation position). Among them, the gradient tree-shaped ABH-DVA produces a minimum

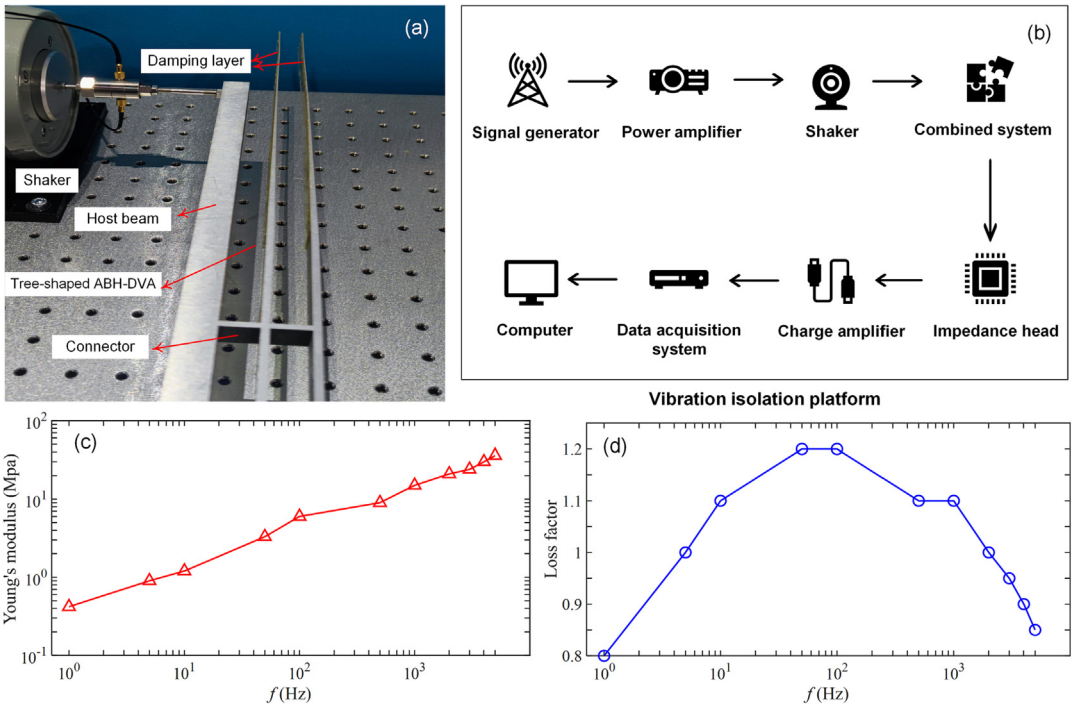

Fig. 18. (a) Experimental set-up, (b) test principle, and (c) the frequency dependence of the Young's Modulus and (d) the associated loss factor of the 3M^{TM} F9473PC tape at 20℃ [41].

reduction of 21.6 dB and an average of 27.3 dB, slightly better than non-gradient tree-shaped ABH-DVA with a minimum reduction of 19.9 dB and an average of 26.4 dB. Both tree-shaped ABH-DVAs far outperform their unilateral counterpart, especially in the very low frequency range. This again confirms that the rich dynamics of the tree-shaped ABH-DVA facilitate the creation of better frequency matching with the host structure, which in turn produces combined damping-controlled and strong interaction-controlled vibration reduction. The fact that no parameter tuning is needed to accommodate different host structures also demonstrates the robustness of the proposed DVAs.

5. Experimental validations

Experiments were then conducted to verify the proposed MSTMM model and the predicted low-frequency and broadband vibration reduction effects. The experimental setup and the test principle are shown in Fig. 18(a) and (b). A tree-shaped ABH-DVA was manufactured through the electro discharge machining method. Both the host beam and the ABH-DVA are made of 7050 aluminum alloy, which has an excellent strength-to-weight ratio. A multilayered 3M^{TM}F9473PC adhesive transfer tape with a total thickness of merely 1.04 mm surface-coats the tapered portion of the ABH-DVA. The frequency-dependent Young's modulus and the loss factor of the tape [41] at the room temperature (20 °C) are used in the theoretical model, as shown in Fig. 18(c) and (d). Other geometrical and material parameters of the combined systems are: $h = 16$ mm,$L = 650$ mm;$h_1 = 3.36$ mm, $h_0 = 0.49$ mm, $L_{ABH} = 260$ mm, $L_1 = L_2 = 70$ mm; $h_c = 2.95$ mm, $L_c = 15.9$ mm; $\rho_a = 2800$ kg/m^3, $E_a = 70.3$ Gpa and $\rho = 1012$ kg/m^3. All structural components have the same width of 20.5 mm.

The host beam was mounted on a rigid metallic clip with its other end free, mimicking a cantilever beam or clamped-free boundary conditions. The attachment position of the ABH-DVA was 60 %L from the clamped end of the host beam. The host structure was excited by a sinusoidal sweep signal at the free end using an electromagnetic shaker (JZK-5). An impedance head (CL-YD-331) with combined force and acceleration sensors was used to measure the input force and the acceleration at the driving point, which were amplified by a charge amplifier (YE5857A-10). The shaker, the transducers and the amplifier are all from the Sinocera Piezotronics, Inc.

The driving point mobilities of the host beam with and without the tree-shaped ABH-DVA are shown in Fig. 19. Generally, a good agreement is observed between the predicted results using MSTMM and the measured ones, demonstrating the correctness

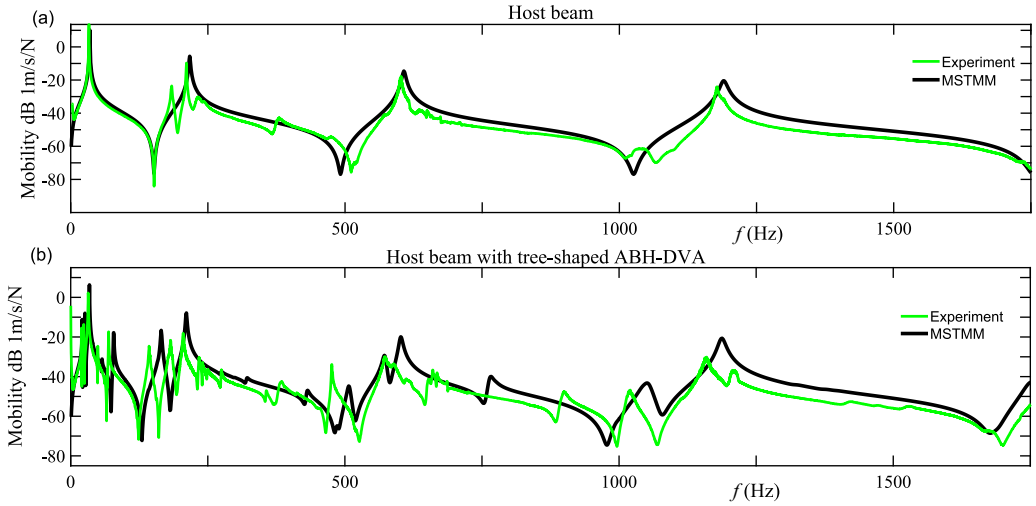

Fig. 19. Comparison of the measured driving point mobility with the predicted one. (a) host beam without tree-shaped ABH-DVA, and (b) host beam with tree-shaped ABH-DVA.

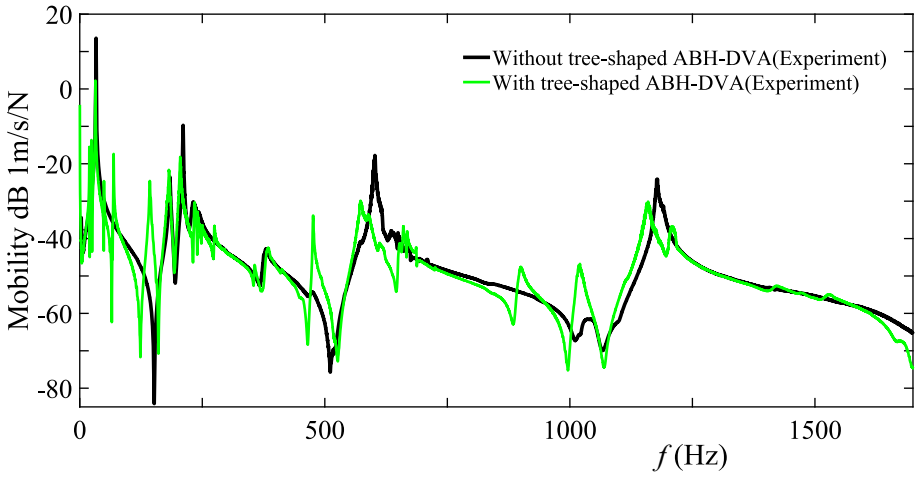

Fig. 20. Comparison of the measured driving point mobility of the host beam with and without the tree-shaped ABH-DVA.

of the proposed method. The slight left-shift of the measured results from the theoretical ones could be attributed to that the Euler-Bernoulli beam theory used in theoretical model neglects the rotational inertia and shear deformation. To better demonstrate the vibration reduction effect of the ABH-DVA, the comparison of the measured driving point mobility of the host beam with and without the tree-shaped ABH-DVA are shown in Fig. 20. It can be observed that, with the introduction of the tree-shaped ABH-DVA, all resonant peaks are suppressed within the entire frequency range concerned, demonstrating the low-frequency and broadband vibration reduction effects of the proposed ABH-DAV design.

6. Conclusions

This study reports the development of an efficient and flexible tool for the simulation and analysis of complex ABH structures, alongside the proposal of a novel tree-shaped ABH-DVA for the mitigation of structural vibration.

An analytical dynamic model based on a multibody system transfer matrix method (MSTMM) is established for dealing with a vibrating structure coupled with an ABH cluster. The MSTMM consists in replacing the global dynamic equations with low-order transfer equations, which features high computational speed, and flexible computational implementation. Using the method, eigenvalues and the steady state vibration response of the combined system can be obtained. The method is demonstrated and validated by COMSOL finite element simulation results of a combined system composed of a host beam structure with a tree-shaped ABH-DVA.

The vibration reduction mechanisms of the tree-shaped ABH-DVA are investigated in terms of the vibrational energy ratio and vibration spatial distribution of the combined system. Results show that in contrast to previous ABH structures, the ABH-DVA as an add-on device could reduce vibration of the host beam both above and below its threshold frequency (TF) through three different physical processes. Below the TF, "interaction-dominated" mechanism prevails since the ABH effects are minimal due to the absence of its local deformation and the ABH-DVA basically acts as a SDOF DVA. Vibration reduction takes place when frequency mating condition is satisfied. Above the TF, the ABH unit starts to deform to produce resonant local modes in the tapered section. As a result, a thin layer of damping material can produce considerable energy loss owing to the emergence of the ABH effects. For the unmatched frequencies, the vibration reduction is caused by "damping-controlled" mechanism or enhanced modal damping due to the ABH-specific energy concentration phenomenon. For the matched frequencies, a greater amount of vibration energy is trapped into the ABH unit due to strong interaction, so the same amount of damping could produce much higher vibration reduction due to "combined interaction and damping" mechanism.

The efficacy of the tree-shaped ABH-DVA for low frequency and broadband vibration reduction can be ensured by designing its threshold frequency as the lower limit of the targeted frequency range. This would create abundant local modes inside the ABH units with high loss factors. Considering the denser modes of proposed tree-shaped ABH-DVAs compared with the unilateral counterpart within the same frequency range, the former delivers extraordinary vibration reduction (minimally 19.9 dB and 21.6 dB respectively for non-gradient and gradient cases studied here) within a broad and low frequency range (25 Hz–2500 Hz), outperforming the latter with the same added weight and damping material. The rather consistent vibration reduction effects observed on three different host beams demonstrate the robustness of the proposed DVA to cope with structural changes in the host structure without tedious tuning process that is usually required by conventional DVAs. The proposed theoretical model using MSTMM and the low-frequency broadband vibration reduction effect are also validated by experimental results.

In a broader sense, this research offers a novel and general approach, alongside the simulation and analysis method, for the design and research of more complex ABH structures with various structure components and topologies.

CRediT authorship contribution statement

Kaixing Huang: Methodology, Validation, Data curation, Writing – original draft. **Yanni Zhang:** Supervision, Conceptualization, Methodology, Writing – review & editing. **Xiaoting Rui:** Supervision, Conceptualization. **Li Cheng:** Conceptualization, Writing – review & editing. **Qinbo Zhou:** Writing – review & editing.

Data availability

Data will be made available on request.

Declaration of Competing Interest

The authors declare that they have no known competing financial interests or personal relationships that could have appeared to influence the work reported in this paper.

Acknowledgements

This work was supported by the National Natural Science Foundation of China (Grant No. 11874303), the Foundation of Equipment Pre-research Area (Grant No. 80910010102) and Shuangchuang Program of Jiangsu Province (Grant No. JSSCBS20210240).

References

[1] Ormondroyd J, Den Hartog JP. The theory of the dynamic vibration absorber. Trans ASME 1928:50.
[2] Liu YZ, Yu DL, Zhao HG, Wen XS. Research progress of passive dynamic vibration absorption technology. J Mech Eng 2007;43:1–8.
[3] Zuo L, Nayfeh SA. Minimax optimization of multi-degree-of-freedom tuned-mass dampers. J Sound Vib 2004;272(3-5):893–908.
[4] Zhu X, Chen Z, Jiao Y. Optimizations of distributed dynamic vibration absorbers for suppressing vibrations in plates. J Low Freq Noise V A 2018;37 (4):1188–200.
[5] Yang C, Li D, Cheng Li. Dynamic vibration absorbers for vibration control within a frequency band. J Sound Vib 2011;330(8):1582–98.
[6] Kerlin RL. Predicted attenuation of the plate-like dynamic vibration absorber when attached to a clamped circular plate at a non-central point of excitation. Appl Acoust 1988;23(1):17–27.
[7] Aida T, Aso T, Nakamoto K, Kawazoe K. Vibration control of shallow shell structures using a shell-type dynamic vibration absorber. J Sound Vib 1998;218(2):245–67.
[8] Wang YQ, Sheng MP, Sun JC. Wideband vibration absorption mechanism of variable cross-section beam dynamic vibration absorber. J Vib Eng (Chinese) 2004;17:1–4.
[9] Ungar EE, Kurzweil L.G. Structural Damping Potential of Waveguide Absorbers, NASA STI/Recon Technical Report N 1984; 86: 21907.
[10] Hettema CD, Shin YS, Kim KS. Viscoelastic Circular Plate Wave Guide Absorber. J Vib Acoust 1991;113:383–6.
[11] Li Xi, Feng D. Research on Plate Viscoelastic Waveguide Absorber. Adv Sci Lett 2012;12(1):285–8.
[12] Shin YS, Watson SJ, Kim KS. Passive Vibration Control Scheme Using Circular Viscoelastic Waveguide Absorbers. J Press Vessel Technol 1993;115:256–61.
[13] Bowyer EP, Krylov VV. Damping of flexural vibrations in turbofan blades using the acoustic black hole effect. Appl Acoust 2014;76:359–65.
[14] Zhou T, Cheng L. A resonant beam damper tailored with Acoustic Black Hole features for broadband vibration reduction. J Sound Vib 2018;430:174–84.
[15] Zhang Y, Chen K, Zhou S, Wei Z. An ultralight Phononic beam with a broad low-frequency band gap using the complex lattice of ABHs. Appl Phys Express 2019;12:077002.

[16] Ma L, Cheng L. Numerical and experimental benchmark solutions on vibration and sound radiation of an Acoustic Black Hole plate. Appl Acoust 2020;163:107223.
[17] Zhang Y, Chen K, Cheng Y, Wei Z. Lightweight-high-stiffness vibration insulator with ultra-broad band using graded double-leaf ABHs. Appl Phys Express 2020;13:017007.
[18] Li H, Sécail-Géraud M, Pelat A, Gautier F, Touzé C. Experimental evidence of energy transfer and vibration mitigation in a vibro-impact acoustic black hole. Appl Acoust 2021;182: 108168.
[19] Li M, Deng J, Zheng L, Xiang S. Vibration mitigation via integrated acoustic black holes. Appl Acoust 2022; 198:109001.
[20] Zhou T, Cheng L. Planar Swirl-shaped Acoustic Black Hole Absorbers for Multi-directional Vibration Suppression. J Sound Vib 2022; 516: 116500.
[21] Krylov VV, Tilman FJBS. Acoustic 'black holes' for flexural waves as effective vibration dampers. J Sound Vib 2004;274(3-5):605–19.
[22] Ji H, Wang N, Zhang C, Wang X, Cheng L, Qiu J. A vibration absorber based on two-dimensional acoustic black holes. J Sound Vib 2021; 500: 116024.
[23] Krylov VV. Conditions for validity of the geometrical-acoustics approximation in application to waves in an acute-angle solid wedge. Soviet Physics Acoustics 1989;35:176–80.
[24] Krylov VV. Localized acoustic modes of a quadratic solid wedge. Moscow Univ Phys Bull 1990;45:65–9.
[25] Georgiev VB, Cuenca J, Gautier F, Simon L, Krylov VV. Damping of structural vibrations in beams and elliptical plates using the acoustic black hole effect. J Sound Vib 2011;330(11):2497–508.
[26] Tang L, Cheng L, Ji H, Qiu J. Characterization of acoustic black hole effect using a one-dimensional fully-coupled and wavelet-decomposed semi-analytical model. J Sound Vib 2016;374:172–84.
[27] Zhu J, Liu Y, Liang Z, Chen T, Li J. Elastic waves in curved space: mimicking a wormhole. Phys rev let 2018;121:234301.
[28] Conlon SC, Fahnline JB, Semperlotti F. Numerical analysis of the vibroacoustic properties of plates with embedded grids of acoustic black holes. J Acoust Soc Am 2015;137(1):447–57.
[29] Ding W, Chen T, Chen C, Chronopoulos D, Zhu J, Assouar B. Thomson scattering-induced bandgap in planar chiral phononic crystals. Mechanical Systems and Signal Processing. 2023;186:109922.
[30] Rui X, Yun L, Lu Y, He B, Wang G. Transfer Matrix Method of Multibody System and Its Application. Beijing, China: Science Press; 2008.
[31] Rui X, Wang G, Zhang J. Transfer matrix method for multibody systems: theory and applications. John Wiley & Sons; 2018.
[32] Rui X, Zhang J, Wang X, Rong B, He B, Jin Z. Multibody system transfer matrix method: The past, the present, and the future. Int J Mech Syst Dyn 2022;2 (1):3–26.
[33] Abbas LK, Zhou Q, Bestle D, Rui X. A unified approach for treating linear multibody systems involving flexible beams. Mech Mach Theory 2017;107:197–209.
[34] Georgiev VB, Cuenca J, Moleron Bermudez MA, Gautier F, Simon L, Krylov VV. Numerical and experimental investigation of the acoustic black hole effect for vibration damping in beams and elliptical plates. Euronoise 2009.
[35] Rui X, Bestle D. Reduced multibody system transfer matrix method using decoupled hinge equations. Int J Mech Syst Dyn 2021;1(2):182–93.
[36] Gu J, Rui X, Zhang J, Chen G, Zhou Q. Riccati Transfer Matrix Method for Linear Tree Multibody Systems. J Appl Mech 2017;84:011008.
[37] Gu J, Rui X, Zhang J, Chen G. Computation of eigenvalues of linear tree multibodysystem based on Riccati transfer matrix method. J Nanjing Univ Sci Technol 2018;42:8–17.
[38] Bestle D, Abbas L, Rui X. Recursive eigenvalue search algorithm for transfer matrix method of linear flexible multibody systems. Multibody Syst Dyn 2014;32(4):429–44.
[39] Den Hartog JP. Mechanical vibrations. 4th ed. New York: McGraw-Hill; 1956.
[40] Denis V, Pelat A, Gautier F, Elie B. Modal Overlap Factor of a beam with an acoustic black hole termination. J Sound Vib 2014;333(12):2475–88.
[41] Liu W, Ewing MS. Experimental and analytical estimation of loss factors by the power input method. AIAA J 2007;45(2):477–84.